Published in final edited form as:
J Nucl Med. 2013 April ; 54(4): 639–646. doi:10.2967/jnumed.112.105742.

Multimodal fluorescence mediated tomography and SPECT/CT for small animals imaging

Metasebya Solomon[1], **Ralph E. Nothdruft**[2], **Walter Akers**[2], **W. Barry Edwards**[2], **Kexian Liang**[2], **Baogang Xu**[2], **Gail P. Suddlow**[2], **Hamid Deghani**[4], **Yuan-Chuan Tai**[2], **Adam T. Eggebrecht**[2], **Samuel Achilefu**[1,2,3], and **Joseph P. Culver**[1,2,5]

[1]Department of Biomedical Engineering, Washington University, St. Louis, MO

[2]Department of Radiology, Washington University School of Medicine, St. Louis, MO

[3]Biochemistry and Molecular Biophysics, Washington University School of Medicine, St. Louis, MO

[4]School of Computer Science, University of Birmingham, Edgbaston, Birmingham B15 2TT, UK

[5]Department of Physics, Washington University, St. Louis, MO

Abstract

Spatial and temporal co-registration of nuclear and optical images would enable the fusion of the information from theses complementary molecular imaging modalities. A critical challenge in integration is fitting optical hardware into the nuclear imaging platforms. Flexible fiber-based fluorescence mediated tomography (FMT) systems provide a viable solution because the various imaging bore sizes of small animal nuclear imaging systems can potentially accommodate the FMT fiber imaging arrays. Further, FMT imaging facilitates co-registering the nuclear and optical contrasts in time. Herein, we combine a fiber based FMT system with a preclinical NanoSPECT/CT platform. Feasibility of in vivo imaging is demonstrated by tracking the accumulation of a monomolecular multimodal imaging agent (MOMIA) in a sentinel lymph node (SLN) of a rat.

Methods—The fiber-based, video-rate FMT imaging system is composed of 12 alternating sources (785nm and 830nm LDs) and 13 detectors. To maintain high temporal sampling, the system simultaneously acquires ratio-metric data at each detector. The data is reconstructed using the normalized Born approach with a three-dimensional finite element model derived from an anatomical CT image of a rat for accurate light propagation modeling. Nuclear and optical contrasts are integrated by using a MOMIA. Data collection begins immediately after injection of the MOMIA intradermally into the forepaw with the FMT data acquired simultaneously with both the SPECT and CT.

Results—Fluorescence and radioactivity from the MOMIA were co-localized in a spatially coincident region. Intravital imaging with surgical exposure of the lymph node validated the localization of the optical contrast. The optical and nuclear contrasts where integrated by incorporating SPECT as a prior in the DOT reconstruction.

Address all correspondence to: Joseph P. Culver, Ph.D, Department of Radiology, Washington University School of Medicine, 4525 Scott Avenue, St. Louis, MO 63110 USA, Tel: 314 747-1341, culverj@wustl.edu.
First Author Address: Metasebya Solomon (Graduate Student (Ph. D Candidate)), Department of Radiology and Biomedical Engineering, Washington University School of Medicine, 4525 Scott Avenue, St. Louis, MO 63110 USA, Tel: 314 747-6353, solomonm@wustl.edu

AUTHOR CONTRIBUTIONS

Conceived and designed the experiments: MS REN WA WBE SA JPC. Performed the experiments: MS WA KL BX GPS. Analyzed the data: MS REN SA JPC. Contributed reagents/materials/analysis tools: MS REN WA WBE KL BX GPS HD YCT ATE SA JPC. Wrote the paper: MS REN WA WBE KL BX GPS HD YCT ATE SA JPC.

Conclusion—The feasibility of integrating a fiber-based, video-rate FMT system with a commercial preclinical NanoSPECT/CT platform was established. The co-localization of the MOMIA in a spatially coincident region on the co-registered FMT-SPECT-CT image may facilitate the development of the next generation preclinical and clinical multimodal optical-nuclear platform for a broad array of imaging applications. Due to the complementary information provided by the SPECT, CT and FMT imaging, this approach has potential to elucidate the underlying biological processes relevant to cancer diagnosis and therapy monitoring.

Multimodal imaging strives to improve upon uni-modal imaging by combining mutliple contrasts. For example, combining anatomic with molecular imaging (PET/CT and SPECT/CT) has provided an anatomical context for the detailed molecular information from the nuclear contrasts (1–3). However, full fusion of the anatomic and molecular information is limited by the relatively weak connection between the different contrasts. Alternatively mutliple molecular contrasts might be joined through specific links (4–6). For example optical methods have unique activation contrast mechanisms, which are complementary to PET/SPECT information and the information available to both nuclear and optical contrasts can be harnessed directly using monomolecular optical multimodality imaging agent's (MOMIA) (4–7). Imaging of MOMIA agents requires suitable instrumentation and algorithms. To combine optical data with PET/SPECT, optical contrasts can be imaged in three dimensions by diffuse optical tomography (DOT) (8–13). In this work, we demonstrate the feasibility of combining a prevoiusly reported fiber-based, video-rate fluorescence mediated tomography (FMT) system (14) with a preclinical NanoSPECT/CT platform (Bioscan, Inc.) for combined optical and nuclear imaging of dynamic events associated with lymphatic transport.

The design and construction of a multimodal imaging platform presents a number of challenges. The first is integrating hardware such that each modality is able to function with minimal, or acceptable, interference from the others. Hardware integration requires compatibility of all the parts for both platforms. The second challenge is spatial and temporal coregistration of information from the disparate reporting strategies under each modality. For instance, the distinct chemical and physical characteristics of traditional contrast agents might lead to different biodistribution and migration rates. MOMIAs are being developed to address these pharmacokinetic issues. Recent work has demonstrated the use of this approach for SPECT/optical (15–17), PET/Optical (6, 7, 18), and MRI/optical (19–21) imaging. The last challenge is determining how to merge the anatomical or functional information from multiple technologies into a single imaging output that leverages the respective strengths of each modality and provide new insight into biological processes relevant to cancer diagnosis and therapy monitoring (4, 11). Such algorithms are currently the subject of intensive research though most of the work is focused on incorporating structural information from X-ray/CT (8, 11, 17) or MRI (19, 22) into DOT reconstructions.

To address the integration of the instrumentation, we took advantage of the flexibility of fiber arrays to provide a compact conduits of light to and from the animal so that the FMT imaging array could fit into the bore of the existing NanoSPECT/CT system without modifications. A goal in this work is to evaluate the degree of influence that the fiber arrays have on the CT and SPECT images. To facilitate integration of the nuclear and optical contrasts, we used a MOMIA based on a radiolabeled near-infrared dye synthesized in our laboratory (6). For a feasibility of in vivo imaging simultaneous mapping of sentinel lymph nodes and phantom studies of different depths was performed with the combined nuclear-optical imaging platform. Fluorescence and radioactivity from the MOMIA was co-localized in the area of the axillary lymph node relative to the site of the injection. Accurate depth localization to MOMIA targets were established in to depths of upto 10 mm. The proposed combined multimodal platform has the potential to become a practical tool for a broad array of imaging applications, ranging from early disease detection to monitoring progress of disease and therapies.

MATERIALS AND METHODS

1.1 Fiber-based FMT Imaging System

DOT source and detector console: Laser diodes with a wavelength of 785 nm (Thorlabs DL7140-201S) (3.5 mW) and 830 nm (Thorlabs HL8325G) (1.5 mW) have dedicated drivers and control lines for each source to allow flexible software configurable source encoding (frequency- and time-encoding). The detection channels use optically-filtered discrete avalanche photodiodes (Hamamatsu C5460-01) digitized with dedicated 24-bit analog-to-digital converters (MOTU HD 192). The narrowband optical filters (CVI) have an 830 +/− 10 nm center wavelength and an out-of-band rejection of OD4, thus blocking the excitation light while passing the fluorescent and reference signals. An aspheric lens is used to collimate the light to optimize the blocking of excitation light by the narrowband interference filter and enhance fluorescent signal detection. With this scheme, we acquire frequency-encoded fluorescence emission and reference transmission (used to normalize the measured fluorescence) light levels concurrently at each detector. This ratiometric data allows DOT reconstructions using the normalized Born approximation, resulting in a map of quantified fluorochrome distribution. All data are acquired at a frame rate of 30 Hz. A total of 108 measurements from optode-pairs representing the 1st2ndand 3rd nearest-neighbors are used for image reconstruction. Further design elements and capabilities of the fiber-based, video-rate FMT are detailed in a previous publication (14).

DOT imaging fiber array: The imaging array is composed of a grid of alternating sources (12) and detectors (13). Light from the sources is coupled into 0.5 numerical aperture with 2.5 mm diameter fiber bundles made of borasilicate glass sheathed with lightweight silicone. The DOT imaging array composed of flexible silicone with right-angle fibers is integrated with the NanoSPECT/CT system.

1.2 SPECT/CT Acquisition

The compatibility test of our fiber-based FMT insert used a NanoSPECT/CT platform (Bioscan, Inc., Washington, D.C.). For NanoSPECT/CT scanning, first, CT was performed (using a 45 KVP energy tube at 177 mA and 180 projections with 400 ms exposure with pitch of 1), followed by helical SPECT of 16 projections with 60 seconds each. CT and SPECT projections were reconstructed using InvivoScope software (Bioscan, Inc., Washington, D.C.). The high-resolution NanoSPECT/CT anatomical and radioactive images have isotropic voxel size of 0.4 and 0.6 mm respectively.

1.3 MOMIA Synthesis

DOTA-Gly-Ser-Gly-Lys(Cypate)-E-Ahx-NH2,LS444, was synthesized and radiolabeled with $^{111}InCl_3$ (MSD-Nordion, Kanata, ON, Canada, 3.0 microcuries (μCi)) in aqueous buffer (190μl, 0.4 M sodium acetate, pH 4.5, 30 min, 98 °C) as described previously (6, 7). Labeling efficiency and radiochemical purity were checked by HPLC (Supelcosil ABZ $^+$ PLUS, HPLC Column, 15cm X 4mm, 5μm) with a gradient of H_2O and acetonitrile containing 0.1% TFA. The radiochemical purities of peptides used in the studies were always above 95%. The specific activity was 223.0 μCi/nmol.

1.4 Experimental Protocol

Animal handling and preparation were performed according to the guidelines approved by the Washington University School of Medicine Animal Studies Committee for humane care and use of laboratory animals. A flowchart of the acquisition timeline is presented in supplemental Fig. 1A. The rats (n=5, 200–250 g Female Sprague Dawley, HSD, Indianapolis, IN) were first anesthetized via a mixture of ketamine and xylazine (85 mg/kg and 15 mg/kg IP). The MOMIA imaging agent (100 μL of ^{111}In-LS444) was then administered via forepaw injection. Concurrent FMT/SPECT/CT imaging was performed immediately after injection.

The DOT imaging fiber array was securely positioned on top of the rat, which was then advanced into the NanoSPECT/CT imaging chamber (Supplemental Fig. 1B). The SPECT/CT scanning regions were selected to include the injection site as well as the DOT imaging pad by top-view topogram. CT was performed followed by helical SPECT, with total acquisition times of 5 and 16 minutes respectively. To evaluate the influence of the DOT array on the SPECT/CT imaging, we also performed SPECT/CT imaging without the DOT fiber array (Supplemental Fig. 1C). After the concurrent FMT/SPECT/CT scanning, the DOT fiber array was removed and the SPECT/CT imaging protocol was repeated.

For reference and verification of ^{111}In-LS444 uptake by the lymph nodes (LNs), reflectance fluorescence images were acquired in vivo before and after removal of overlying skin following euthanasia using the near-infrared (NIR) reflectance fluorescence system (Pearl, LiCor Biosciences, Lincoln, NE). Fluorescence and brightfield microscopy images of the excised LNs were acquired using Olympus BX51 upright epifluorescence microscope (Olympus America, Center Valley, PA) (See supplemental data).

To evaluate the performance of the system as a function of depth we followed the approach we used for the stand alone FMT system, but in this instance with MOMIA targets. Targets of 3 mm diameter plastic tube filled with the MOMIA agent were prepared and embedded at 4, 7, 10 mm depth in a tissue mimicking phantom with $\mu_a = 0.19\ \text{cm}^{-1}$ and $\mu'_s = 3.4\ \text{cm}^{-1}$. The tissue mimicking phantom was constructed by mixing agarose (Sigma-Aldrich, Saint Louis, Missouri) with intralipid (20% fat emulsion, Fresenious Kabi, Germany), and India ink (Speedball, Statesville, North Carolina) to obtain the appropriate absorption and scattering properties. The mixture was poured into a mold and allowed to solidify at room temperature. The imaging protocol described above is implemented to acquire optical and nuclear datasets of the different phantoms.

1.5 Fluorescence DOT Reconstruction

We generated a subject-specific three-dimensional (3D) finite-element model (FEM) (Fig. 1). Using an anatomical image of a rat obtained from an X-ray CT (Fig. 1A), we created a tetrahedral mesh using Mimics™ with a maximum inter-nodal distance both on the surface and within the mesh volume of 1 mm. The mesh, composed of 400,399 linear tetrahedral elements connected by 67931 nodes, was segmented into two tissue types: bone and soft tissues and assigned their corresponding optical properties ($\mu_a = 0.17\ \text{cm}^{-1} \mu'_s = 24\ \text{cm}^{-1}$ and $\mu_a = 0.19\ \text{cm}^{-1} \mu'_s = 34\ \text{cm}^{-1}$ respectively) (Figs. 1C and D). A heterogeneous tissue model was employed because previous studies that have shown improvements relative to light models that assume homogeneous optical properties (23–26). For the tissue phantom imaging, we used the X-ray CT image and created a homogeneous mesh and assigned the corresponding optical properties ($\mu_a = 0.19\ \text{cm}^{-1} \mu'_s = 34\ \text{cm}^{-1}$). A second anatomical CT image of each rat and the tissue mimicking phantom was obtained with DOT fibers in place and was used to obtain the 3D coordinates of the optode positions from Matlab™ manually (Fig. 1B). An affine transform was performed to bring the FEM mesh into CT space for co-registering the sources and detectors locations (Fig. 1E).

The light transport was then modeled using NIRFAST following our previously reported methods (27). Briefly, an adjoint approach to constructing the Jacobian was used to construct a sensitivity matrix. The construction of the sensitivity matrix specific to fluorescence imaging follows the methods previously described (see reference (14)). The sensitivity matrix maps the relationship between the optical parameters (fluorescence distribution) for all voxels as a function of the chosen source-detector arrangement (28) following the normalized Born approach (14). We directly invert the sensitivity matrix via a Moore-Penrose generalized inverse (29, 30). The experimental source-detector measurements are converted into images by matrix multiplication with the inverted matrix. The recovered fluorescence yield of the tissue at each FEM node is then presented in 3D. The mesh nodes are then transformed to a voxellated three dimensional space of 1 mm isotropic voxel space for integration with CT/SPECT (a point spread function of the FMT system is ~1.2 cm at 1 cm depth (14)).

The accuracy of the reconstructed FMT image is further improved by using the radioactivity measurement obtained from NanoSPECT/CT as a spatial priori to create a binary mask. The mask is then multiplied with the simulated light propagation matrix (sensitivity matrix) to constrain the DOT image reconstruction.

1.6 Quantification of The Influence of FMT Fibers on SPECT and CT

We evaluated the potential for the presence of the optical fibers to negatively impact the imaging performance of the CT/SPECT imaging systems. The influence of the optical fibers on the transmitted x-ray depends on the linear attenuation coefficient (μ) of glass fibers at a given energy window and the thickness of the fiber arrays (*l*) (Supplemental Fig 1C). The fraction of the transmitted x-ray beam is calculated using the following equation:

$I = I_0 e^{-\mu \cdot l}$; where I_o and I are the incident and the transmitted X-ray beams respectively and *l* is the effective thickness of the glass fiber elements.

In addition, the normalized root mean square error (NRMSE) is used to quantify the distortions induced in the nuclear data due to the presence of the optical fibers:

$NRMSE = \frac{\sqrt{\frac{(X - X_{ref})^2}{N}}}{\max(X_{ref})}$; where X is the nuclear image with DOT fiber array and X_{ref} is the reference image without the optical fibers. N is the total number of image pixels. NRMSE is computed for both the SPECT and X-ray CT datasets.

1.7 Quantifying Image Quality: Localization Accuracy

The localization accuracy of the FMT reconstruction compared to their corresponding SPECT datasets was evaluated by calculating the absolute error in the center of masses' (of the contrast) of the lymph node volumes. The mean fluorescence and radioactivity intensity values in the xyz-planes were computed for each subject from the reconstructed nuclear and optical datasets to compute the center of masses (COMs). In addition, the absolute error of the COMs was computed to assess the positional change between the fluorescence and radioactive distributions. The COMs and COMs error of the reconstructed MOMIA tubes were also computed by averaging the fluorescence and radioactive intensity values for each experimental depth. In addition, quantitative comparison of the difference in spatial resolution was quantified by comparing volumetric ratio of the ROIs between the nuclear and optical datasets of the various depths of the reconstructed tubes.

RESULTS

The goal of this study was to demonstrate the feasibility of combining fiber-based FMT with NanoSPECT/CT. This combined nuclear-optical platform obtained data from both contrast mechanisms concurrently in space and time. Signal from a monomolecular multimodal imaging agent (MOMIA), ^{111}In-LS444, was used to facilitate the spatial integration of the nuclear and optical data.

The potential influence of the optical fibers on the nuclear imaging datasets was evaluated both by computing the X-ray beam attenuation due to glass fibers and, more directly, by measuring the variance introduced into the CT and SPECT signals by the DOT fiber array. The computed results of the percent transmission of the X-ray beam matches the trends of the theoretical estimates based on attenuation coefficients (energy dependent) of the glass fiber (Table 1). Model calculations estimate the X-ray beam transmission through the fiber array to be 31% and 68 % for the CT (45 keV) and the SPECT (245 keV) datasets respectively.

The measurements of the NRMSE also demonstrated the existence of distortion introduced by the optical fibers (Fig. 2A) in the nuclear data. The NRMSE between the X-ray CT anatomical image with and without FMT imaging fibers (Figs. 2B and 2C) is 8.5%. The NRMSE between the radioactive datasets acquired at the presence (Fig. 2D), and absence (Fig. 2E) is found to be 3.1 +/− 1.3 %, which also accounts for the additional MOMIA accumulated in SLNs during the process of acquiring the reference SPECT measurements. For improved visual reference, the fluorescence and radioactive data measurements are co-registered and displayed on anatomical x-ray CT obtained after removing the DOT fiber arrays (Fig. 2E) for the remainder of the manuscript.

The co-registered molecular information with its corresponding anatomical structure, Fig. 3, demonstrates the feasibility of obtaining measurements with FMT and SPECT molecular contrasts and structural information with x-ray CT. An anatomical x-ray CT of a rat provides structural information that facilitates segmentation of different tissue types. After creating a segmented mesh with MIMICS™, derived from an x-ray CT image, into bone and soft-tissue, their corresponding optical properties are assigned for accurate simulation of light propagation in an inhomogeneous domain to improve DOT image reconstruction (Fig. 1).

Reconstructed FMT images show uptake of the MOMIA by the LNs in the axillary region, as shown with the combined anatomical X-ray CT data (Fig. 3A). The localized radioactive signal in the axillary region of the SPECT/CT image also demonstrated the uptake of the MOMIA by the axillary LNs (Fig. 3B). The high radioactive signals on the left forepaw, the injection site, show the starting point of the lymph tract that leads to the axillary nodes. Due to the limited field of view of the fluorescence DOT fiber array the injection site is not visible in the reconstructed DOT image.

The uptake of ^{111}In-LS444 by the axillary LNs was further validated by combining the SPECT and FMT datasets. The co-registered FMT/SPECT/CT images, Fig 4A, demonstrate co-localization of the multimodal agent in a spatially coincident region. The co-localization confirms that the radioactive and fluorescent signals originate from the same location corresponding to the LNs. The low overlap percentage can be attributed to the difference in resolution (or point spread function) between the optical and nuclear imaging systems and the presence of fractional component of non-radiolabeled LS444. However, the free LS444 fractional component is expected to be very minimal due to the high radiochemical purities of peptides used.

Having demonstrated the co-localization of the fluorescence and radioactive distribution, we explored a simple method to incorporate the high resolution NanoSPECT/CT radioactive data into the DOT image reconstruction to improve the localization and magnitude accuracy of the axillary lymph node signal. A binary mask, created from the radioactivity distribution of the SPECT data was multiplied with the simulated light propagation matrix to constrain the FMT image reconstruction. The SPECT/CT measurements fused with constrained reconstructed FMT datasets, Fig. 4B, demonstrated an improvement incongruency of the radioactive and fluorescence signal in the axillary regions. As a result of using SPECT as a hard prior, the overlap between DOT and SPECT is inherently unity. Likewise it is assumed that the fluorescent signal originates from conjugated complexes and not from free optically active fragments. A soft prior approach to relax these conditions is suggested below. The average spatial discrepancy between the COM of the optical and nuclear datasets for all five rats was 2.68 +/− 1.0 mm and 1.33 +/− 0.85 mm before and after incorporating SPECT as a priori respectively.

Images of the MOMIA targets in tissue mimicking phantoms confirm the localization of the targets in the range of the depths from 5–10 mm (Supplemental Fig 3, Tables 1 2). The average absolute error between the COM of the optical and nuclear datasets for all 3 depths was 4.1 +/− 2.1 mm. The depth dependent spread of the volume of the FMT compared to the SPECT is 2.4 +/− 0.95 after thresholding at 30% maximum.

DISCUSSION

The multimodal optical-nuclear platform shown has the potential to elucidate underlying biological mechanisms relevant to a wide array of diseases. We established the feasibility of integrating a fiber-based, video-rate FMT system with a preclinical NanoSPECT/CT platform. We used our recently developed MOMIA, which has the unique structural feature that both signals (fluorescence and radioactivity) emanate from the same source. The NIR fluorescent molecular probe served as a contrast agent for FMT, while the ^{111}ln served as a source of signal for SPECT imaging to facilitate the fusion of the optical and nuclear datasets with high spatial precision.

In this study we evaluated the FMT-SPECT-CT system for imaging LNs in rats. CT provided well defined anatomy and the combined FMT-SPECT demonstrated co-localization of a MOMIA in a spatially coincident region. We further demonstrated the congruency of the co-localization by incorporating SPECT as a prior in the DOT reconstruction. The average spatial discrepancy in the COMs of the contrasts between SPECT and FMT improved from 2.68 +/− 1.0 mm to 1.33 +/− 0.85 mm after incorporating SPECT into the FMT reconstruction.

Images from separately acquired optical with nuclear platforms has been integrated previously (12, 13). For instance, Nahrendurfet et. al. demonstrated the similarity between FMT and PET by combining the two datasets acquired sequentially on two different scanners using fiducial markers to co-register the data (13). A strength of the current simultaneous optical-nuclear system is that it avoids potential misalignment of datasets due to involuntary non-uniform movement of tissues during repositioning. Furthermore the datasets in the current study are co-registered in time. The first small animal study where optical imaging (scan rate not reported) was physically integrated into a PET system was reported by Li et al. (12). Localization of the tumor with simultaneously acquired nuclear and optical datasets was performed after injection of two separate contrast agents (for fluorescent and radioactive detections) at different time points, separated by 24 hours, thus the datasets were not co-registered in time. Further, acquisition of the anatomical information using a different scanner might lead to co-registration error of the functional molecular data with reference anatomy. To a significant extent, the system presented in this paper addresses many of these difficulties by combing three modalities (FMT-SPECT-CT) within a single device. The FMT-SPECT-CT platform acquires the different functional (fluorescent and radioactive) and anatomical images either simultaneously or sequentially without moving the subject from the bed. This design essentially eliminates differences in subject positioning and also minimizes misalignment due to involuntary internal organ motion.

While the current study does not focus on the dynamics of the lymph node accumulation, we have previously reported the capability of the system for dynamic imaging by monitoring and generating time-course data of the lymphatic dynamics for indocyanine green (ICG) (14). Accumulated dye in the region of the SLN of a rat was imaged to a depth of 10–12 mm over a 10 minute time course. Future studies are needed to explore the imaging of pharmacokinetics and pharamcodynamics for multimodal contrast agents.

Optical imaging can leverage the SPECT and CT information to improve accuracy during data processing and image reconstruction (10, 32). For instance, we generated a small animal 3D finite-element model (FEM) using the anatomical images obtained from an X-ray CT to improve forward modeling of light propagation. In addition, incorporating SPECT data into the fluorescence DOT reconstruction augmented the localization accuracy. An important future area of work is in developing algorithms to incorporate the SPECT data as a soft-prior in the DOT reconstruction to optimize the fusion of the two data types (10).

The current FMT system setup has high dynamic range and linear response and accurate localization at various depths as shown with phantom studies. However, several potential improvements of the fiber-based, video-rate FMT system can still be identified. For instance, the sensitivity of the optical imaging in general is expected to decline with imaging depth, while SPECT has no depth limitation and easily extends to whole-body imaging. Possible extensions on the current design include extending the FMT field of view for more complete coverage. The DOT imaging array shape and size can be designed based on application. For instance, the imaging array could have a cylindrical shape with extended sources and detectors for whole-body imaging. The potential for an expanded fiber array system with up to 48 sources and 48 detectors has been demonstrated for brain imaging in humans (33). A higher-density imaging array could also potentially increase the resolution, particularly at the shallower depths for accurate localization of the target (34). A second limitation is the existence of distortion/artifacts on the x-ray CT images due to the presence of the FMT fiber array and the high attenuation coefficient of borasilicate glass fibers compared to bone. The possibility of whether switching to optical fibers composed of materials with lower attenuation than bone would reduce the artifacts remains a question for future investigation.

Another area of future work is to leverage the complementary contrast mechanisms of SPECT/FMT to evaluate biological mechanisms. MOMIA’s that use activatable optical contrast mechanisms provide complementary information to the "always-on" SPECT information. SPECT can be used for whole-body imaging to localize the diseased tissue based on maps of the concentration of molecular targeted imaging agents while the FMT would report local molecular events, such as enzymatic activity, to monitor therapeutic response (15, 16).

CONCLUSION

We demonstrated integration of a fiber-based, video-rate fluorescence mediated tomography system with a preclinical NanoSPECT/CT platform. The video-rate FMT can accommodate the various imaging bore sizes of nuclear imaging systems due to the flexibility of the imaging fiber array. We used a monomolecular multimodal imaging agent such that the nuclear and optical signals emanated from the same regions to facilitate the fusion of both datasets with high spatial precision. We used the anatomical X-ray CT to generate a small animal 3D finite-element model for light propagation. Co-registered in vivo imaging in rat was performed in the region of the SLN after injection into the lymphatic system via a forepaw injection. Co-localization of the MOMIA in both the FMT and SPECT contrasts was demonstrated. We also observed improvement in spatial correlation of the co-registered datasets after incorporating SPECT as prior to constrain the DOT image reconstruction. The average spatial discrepancy between FMT and SPECT in the COM of the imaging contrasts improved from 2.68 +/− 1.0 mm to 1.33 +/− 0.85 mm after incorporating the SPECT prior into the DOT reconstructions. These results suggest that integrated multimodal FMT/SPECT/CT has the potential to become a powerful and practical tool for a broad array of real time imaging applications.

Supplementary Material

Refer to Web version on PubMed Central for supplementary material.

Acknowledgments

This research was supported in part by the Network for Translational Research U54CA136398 TSP-3 (Culver) and U54CA136398 TSP-1 and R01EB008458 (Achilefu). Dr. Akers is supported by an award from the National Center for Research Resources (K01RR026095).

REFERENCES

1. Alberini JL, Edeline V, Giraudet AL, et al. Single Photon Emission Tomography/Computed Tomography (SPET/CT) and Positron Emission Tomography/Computed Tomography (PET/CT) to Image Cancer. J Surg Oncol. 2011 May 1; 103(6):602–606. [PubMed: 21480254]
2. Even-Sapir E, Keidar Z, Bar-Shalom R. Hybrid Imaging (SPECT/CT and PET/CT)-Improving the Diagnostic Accuracy of Functional/Metabolic and Anatomic Imaging. Semin Nucl Med. 2009 Jul; 39(4):264–275. [PubMed: 19497403]
3. Patton JA, Townsend DW, Hutton BF. Hybrid Imaging Technology: From Dreams and Vision to Clinical Devices. Semin Nucl Med. 2009 Jul; 39(4):247–263. [PubMed: 19497402]
4. Achilefu S, Ye YP, Bloch S, Zhang ZR, Berezin M, Liang KX. Development of contrast effectors for optical and multimodal imaging of tumors. Abstr Pap Am Chem S. 2004 Aug 22.228:U824–U824.
5. Edwards WB, Akers WJ, Ye Y, et al. Multimodal imaging of integrin receptor-positive tumors by bioluminescence, fluorescence, gamma scintigraphy, and single-photon emission computed tomography using a cyclic RGD peptide labeled with a near-infrared fluorescent dye and a radionuclide. Molecular imaging. 2009 Mar-Apr;8(2):101–110. [PubMed: 19397855]
6. Zhang ZR, Liang KX, Bloch S, Berezin M, Achilefu S. Monomolecular multimodal fluorescenceradioisotope imaging agents. Bioconjugate Chem. 2005 Sep-Oct;16(5):1232–1239.
7. Zhang ZR, Achilefu S. Spectral properties of pro-multimodal imaging agents derived from a NIR dye and a metal chelator. Photochem Photobiol. 2005 Nov-Dec;81(6):1499–1504. [PubMed: 16120005]
8. Barber WC, Lin Y, Nalcioglu O, Iwanczyk JS, Hartsough NE, Gulsen G. Combined Fluorescence and X-Ray Tomography for Quantitative In Vivo Detection of Fluorophore. Technology in Cancer Research & Treatment. 2010 Feb; 9(1):45–52. [PubMed: 20082529]
9. Cao L, Breithaupt M, Peter J. Geometrical co-calibration of a tomographic optical system with CT for intrinsically co-registered imaging. Phys Med Biol. 2010 Mar 21; 55(6):1591–1606. [PubMed: 20164534]

10. Cao L, Peter J. Bayesian reconstruction strategy of fluorescence-mediated tomography using an integrated SPECT-CT-OT system. Phys Med Biol. 2010 May 7; 55(9):2693–2708. [PubMed: 20400809]
11. Culver J, Akers W, Achilefu S. Multimodality molecular imaging with combined optical and SPECT/PET modalities. J Nucl Med. 2008 Feb; 49(2):169–172. [PubMed: 18199608]
12. Li CQ, Yang YF, Mitchell GS, Cherry SR. Simultaneous PET and Multispectral 3-Dimensional Fluorescence Optical Tomography Imaging System. Journal of Nuclear Medicine. 2011 Aug 1; 52(8):1268–1275. [PubMed: 21810591]
13. Nahrendorf M, Keliher E, Marinelli B, et al. Hybrid PET-optical imaging using targeted probes. P Natl Acad Sci USA. 2010 Apr 27; 107(17):7910–7915.
14. Solomon M, White BR, Nothdruft RE, et al. Video-rate fluorescence diffuse optical tomography for in vivo sentinel lymph node imaging. Biomed Opt Express. 2011; 2(12):3267–3277. [PubMed: 22162817]
15. Edwards WB, Akers WJ, Ye YP, et al. Multimodal Imaging of Integrin Receptor-Positive Tumors by Bioluminescence, Fluorescence, Gamma Scintigraphy, and Single-Photon Emission Computed Tomography Using a Cyclic RGD Peptide Labeled with a Near-Infrared Fluorescent Dye and a Radionuclide. Molecular imaging. 2009 Mar-Apr;8(2):101–110. [PubMed: 19397855]
16. Lee H, Akers WJ, Cheney PP, et al. Complementary optical and nuclear imaging of caspase-3 activity using combined activatable and radio-labeled multimodality molecular probe. Journal of biomedical optics. 2009 Jul-Aug;14(4):040507. [PubMed: 19725712]
17. Zhang Q, Brukilacchio TJ, Li A, et al. Coregistered tomographic x-ray and optical breast imaging: initial results. J Biomed Opt. 2005 Mar-Apr;10(2)
18. Berezin MY, Guo K, Teng B, et al. Radioactivity-Synchronized Fluorescence Enhancement Using a Radionuclide Fluorescence-Quenched Dye. J Am Chem Soc. 2009 Jul 8.131(26):9198. -+. [PubMed: 19514722]
19. Gulsen G, Yu H, Wang J, et al. Congruent MRI and near-infrared spectroscopy for functional and structural imaging of tumors. Technol Cancer Res Treat. 2002 Dec; 1(6):497–505. [PubMed: 12625777]
20. Guo K, Berezin MY, Zheng J, et al. Near infrared-fluorescent and magnetic resonance imaging molecular probe with high T-1 relaxivity for in vivo multimodal imaging. Chem Commun. 2010; 46(21):3705–3707.
21. Ntziachristos V, Yodh AG, Schnall MD, Chance B. MRI-guided diffuse optical spectroscopy of malignant and benign breast lesions. Neoplasia. 2002 Jul-Aug;4(4):347–354. [PubMed: 12082551]
22. Barbour RL, Graber HL, Chang JW, Barbour SLS, Koo PC, Aronson R. MRI-guided optical tomography: Prospects and computation for a new imaging method. Ieee Comput Sci Eng. 1995 Win;2(4):63–77.
23. Niedre MJ, Turner GM, Ntziachristos V. Time-resolved imaging of optical coefficients through murine chest cavities. Journal of biomedical optics. 2006 Nov-Dec;11(6):064017. [PubMed: 17212540]
24. Dehaes M, Grant PE, Sliva DD, et al. Assessment of the frequency-domain multi-distance method to evaluate the brain optical properties: Monte Carlo simulations from neonate to adult. Biomed Opt Express. 2011; 2(3):552–567. [PubMed: 21412461]
25. Heiskala J, Pollari M, Metsaranta M, Grant PE, Nissila I. Probabilistic atlas can improve reconstruction from optical imaging of the neonatal brain. Opt Express. 2009 Aug 17; 17(17): 14977–14992. [PubMed: 19687976]
26. Eggebrecht AT, White BR, Ferradal SL, et al. A quantitative spatial comparison of high-density diffuse optical tomography and fMRI cortical mapping. NeuroImage. 2012 Feb 10; 61(4):1120–1128. [PubMed: 22330315]
27. Dehghani H, Srinivasan S, Pogue BW, Gibson A. Numerical modelling and image reconstruction in diffuse optical tomography. Philos T R Soc A. 2009 Aug 13; 367(1900):3073–3093.
28. Ntziachristos V, Weissleder R. Experimental three-dimensional fluorescence reconstruction of diffuse media by use of a normalized Born approximation. Optics letters. 2001 Jun 15; 26(12): 893–895. [PubMed: 18040483]

29. Culver JP, Siegel AM, Stott JJ, Boas DA. Volumetric diffuse optical tomography of brain activity. Optics letters. 2003 Nov 1; 28(21):2061–2063. [PubMed: 14587815]
30. Culver JP, Durduran T, Furuya D, Cheung C, Greenberg JH, Yodh AG. Diffuse optical tomography of cerebral blood flow, oxygenation, and metabolism in rat during focal ischemia. J Cereb Blood Flow Metab. 2003 Aug; 23(8):911–924. [PubMed: 12902835]
31. Kapteijn BA, Nieweg OE, Muller SH, et al. Validation of gamma probe detection of the sentinel node in melanoma. J Nucl Med. 1997 Mar; 38(3):362–366. [PubMed: 9074518]
32. Li A, Miller EL, Kilmer ME, et al. Tomographic optical breast imaging guided by threedimensional mammography. Applied Optics. 2003 Sep; 42(25):5181–5190. [PubMed: 12962399]
33. White BR, Snyder AZ, Cohen AL, et al. Resting-state functional connectivity in the human brain revealed with diffuse optical tomography. NeuroImage. 2009 Aug 1; 47(1):148–156. [PubMed: 19344773]
34. Culver JP, Ntziachristos V, Holboke MJ, Yodh AG. Optimization of optode arrangements for diffuse optical tomography: A singular-value analysis. Opt Lett. 2001 May 15; 26(10):701–703. [PubMed: 18040425]

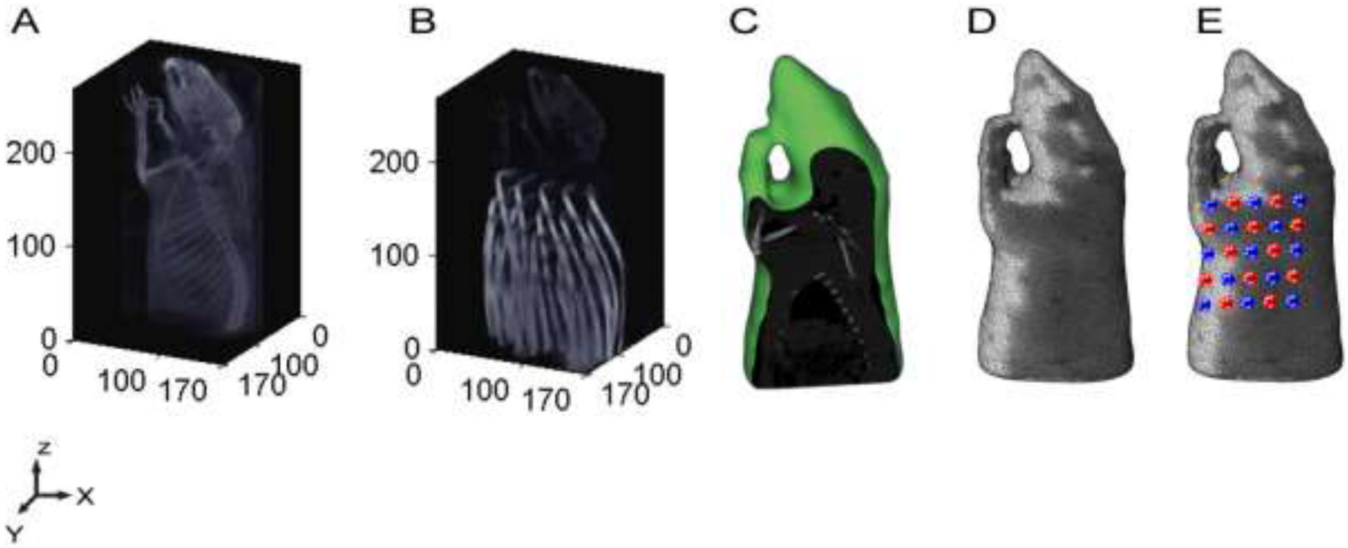

Figure 1.

Fluorescence DOT Image Reconstruction. (A) An X-ray CT is used to capture the three dimension structure of the anatomy of a rat. (B) X-ray CT image with the fiber array of DOT used to obtain optode positions. (C) Sagittal section of the anatomical X-ray CT image after segmentation into bone and soft-tissue region using Mimics™. (D) 3D finite element model (FEM) of small animal half-body mesh generated from CT within Mimics™ to be used for forward modeling of light propagation.(E) Small animal mesh after projection of the optodes (source (red) and detector (blue)). Sensitivity matrix is then generated using with the mesh and the measurement parameters as the main inputs for the FEM modeling of light in tissue using NIRFAST (Dartmouth).

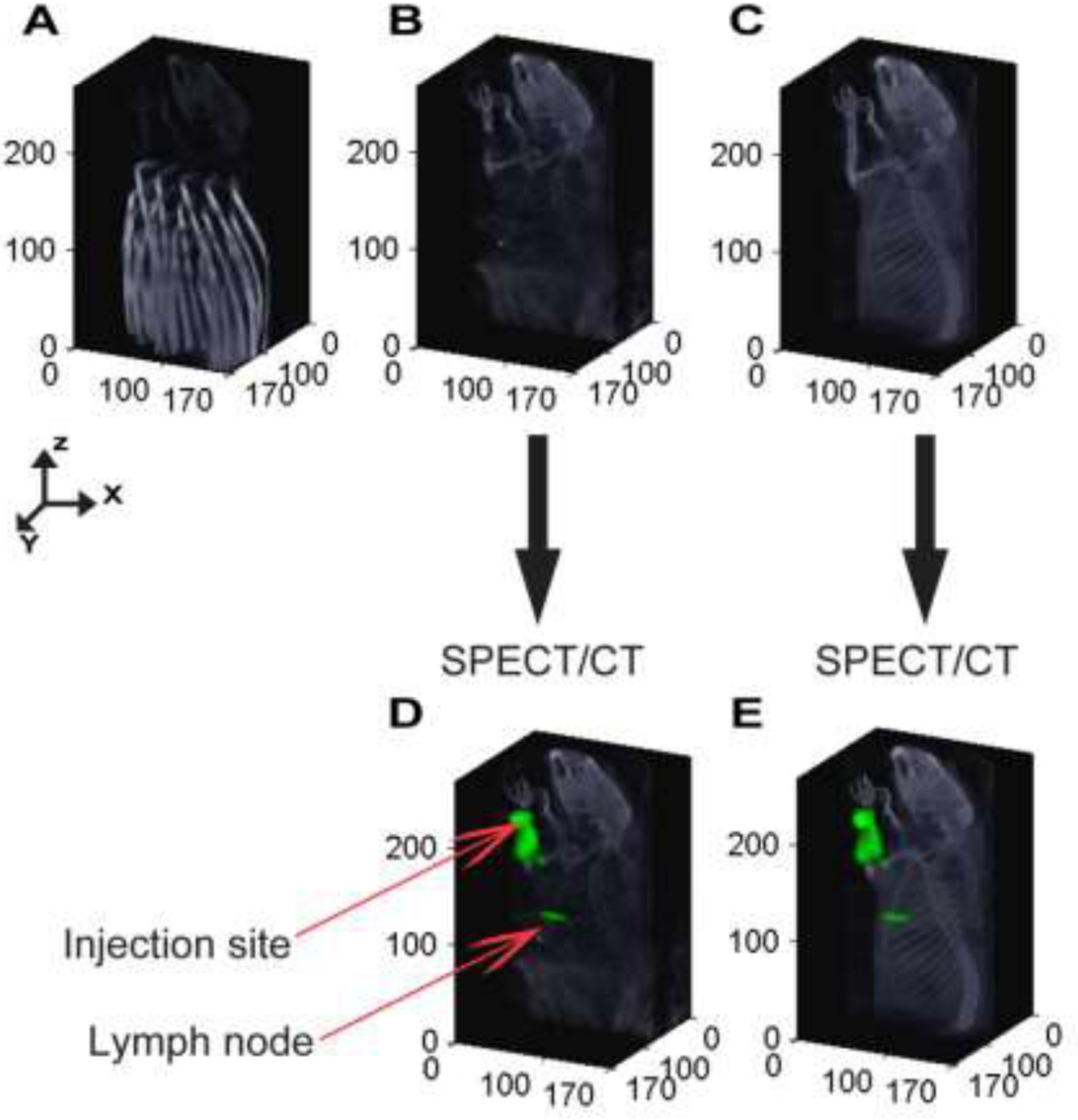

Figure 2.

Evaluating the influence of fiber arrays on SPECT and CT images: (A) X-ray CT image of a rat with the fiber array of DOT. (B) X-ray CT image of the same rat shown after removing the voxels related to the fiber array of the DOT. (C) X-ray CT acquired after removing the DOT imaging pad. The anatomical structures acquired without the fibers are used to display the fluorescence and radioactive distribution for all 5 rats. (D) SPECT data acquired at the presence of DOT fiber array depth in a rat following injection of multimodal imaging agent, ^{111}In-BS255, into the left forearm. (E) SPECT data of the same rat acquired after removing the fibers.

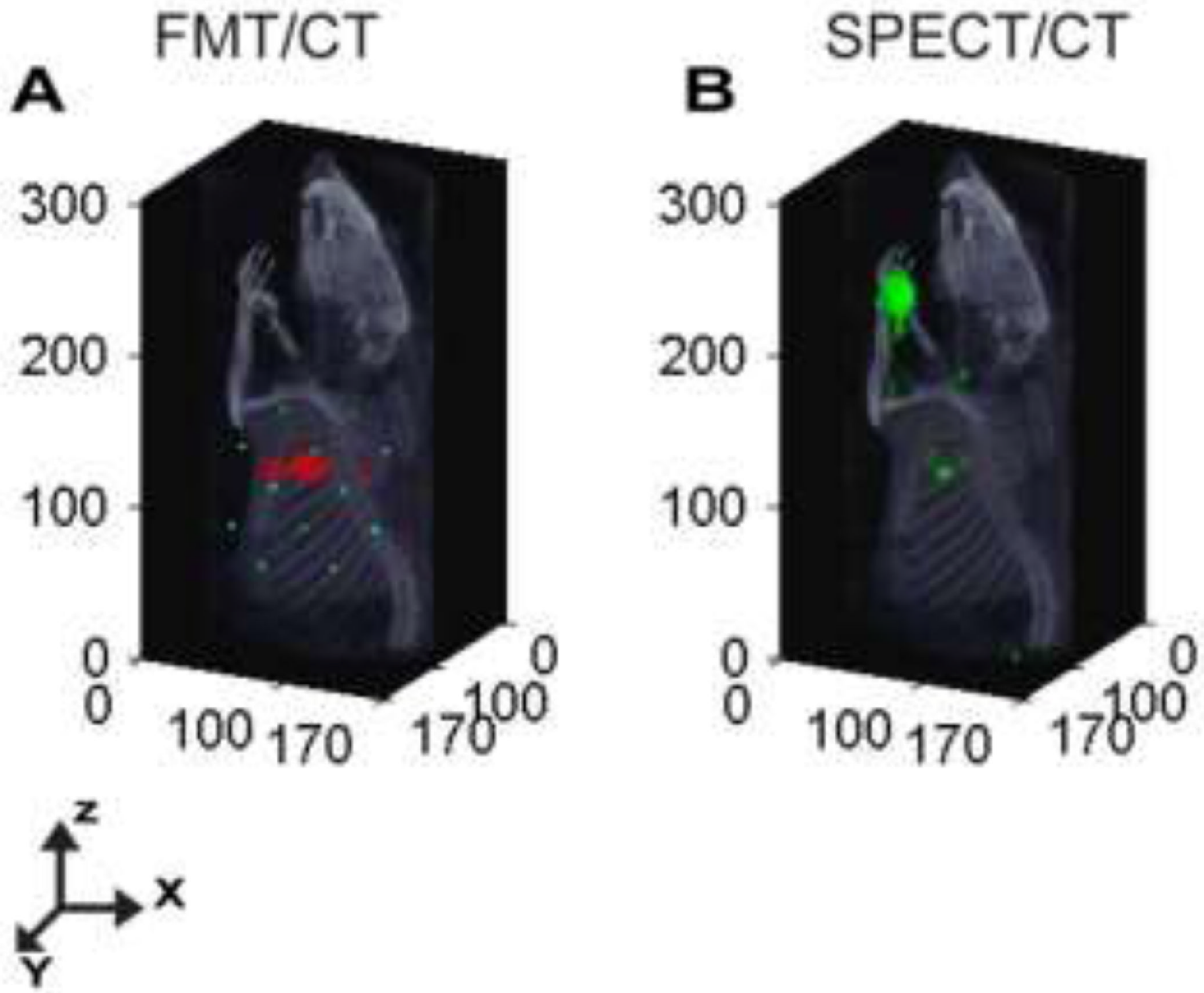

Figure 3.

Representative Sentinel Lymph Node Mapping using Optical and Nuclear Imaging Systems. (A) DOT-CT image of the fluorescent LNs shown at 2mm depth in a rat following injection of multimodal imaging agent, ^{111}In-BS255, into the left forearm. (B) SPECT-CT image demonstrating localization of axillary lymph node identified by accumulation of the multimodal imaging agent.

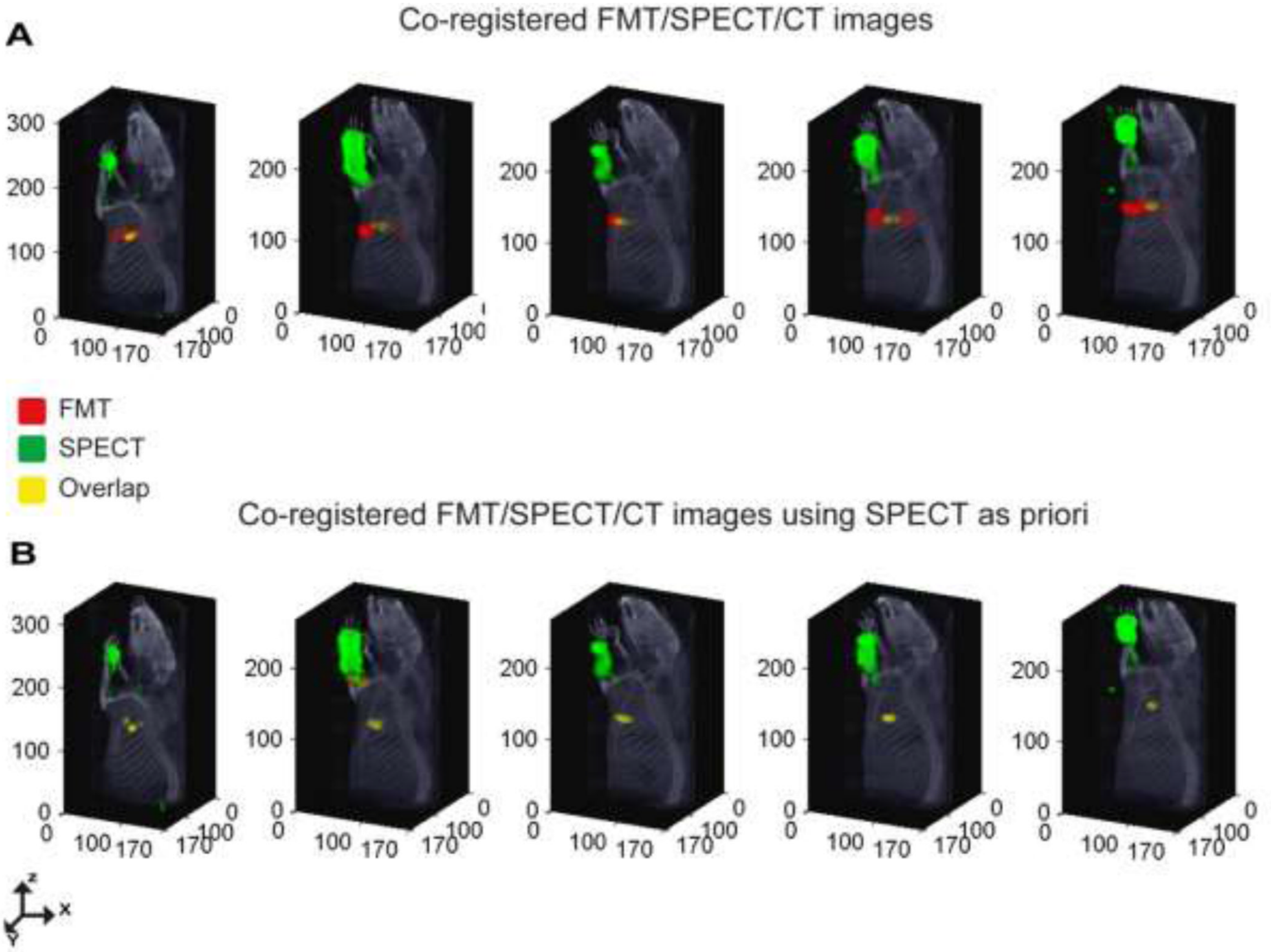

Figure 4.
Multimodal Sentinel Lymph Node Imaging. (A) Co-registered FMT-SPECT-CT image demonstrate co-localization of the MOMIA in spatially coincident region in 5 rats. (B) Demonstrate robust co-localization on the co-registered FMT-SPECT-CT image after using SPECT as a prior.

Table 1

Evaluation the effect of fluorescence DOT fiber arrays on the transmitted X-ray beams of the nuclear imaging system.

	SPECT	**CT**
Radiation Energy (E)	245 keV (^{111}In)	45 keV
Attenuation coefficient of glass, μ(E), cm^{-1}	0.256	0.781
Thickness (l) in cm	1.5	1.5
Transmission [%]	68	31